HHS Public Access

Author manuscript

Phys Med Biol. Author manuscript; available in PMC 2019 October 02.

Published in final edited form as:

Phys Med Biol. ; 63(19): 195016. doi:10.1088/1361-6560/aadf25.

The impact of secondary fragments on the image quality of helium ion imaging

Lennart Volz[#1,2], **Pierluigi Piersimoni**[#1], **Vladimir A. Bashkirov**[3], **Stephan Brons**[4], **Charles-Antoine Collins-Fekete**[5], **Robert P. Johnson**[6], **Reinhard W. Schulte**[3], and **Joao Seco**[1,2]

[1]German Cancer Research Center (DKFZ) Heidelberg, Baden-Württemberg, GE

[2]Heidelberg University, Department of Physics and Astronomy, Heidelberg, Baden-Württemberg, GE

[3]Department of Basic Sciences, Division of Biomedical Engineering Sciences, Loma Linda University, Loma Linda, California, USA

[4]Heidelberg Ion-Beam Therapy Center (HIT), Heidelberg, GE

[5]Chemical, Medical and Environmental Science, National Physics Laboratory, Teddington, UK

[6]SCIPP, University of California at Santa Cruz, Santa Cruz, California, USA

[#] These authors contributed equally to this work.

Abstract

Single-event ion imaging enables the direct reconstruction of the relative stopping power (RSP) information required for ion-beam therapy. Helium ions were recently hypothesized to be the optimal species for such technique. The purpose of this work is to investigate the effect of secondary fragments on the image quality of helium CT (HeCT) and to assess the performance of a prototype proton CT (pCT) scanner when operated with helium beams in Monte Carlo simulations and experiment.

Experiments were conducted installing the U.S. pCT consortium prototype scanner at the Heidelberg Ion-Beam Therapy Center (HIT). Simulations were performed with the scanner using the TOPAS toolkit. HeCT images were reconstructed for a cylindrical water phantom, the CTP404 (sensitometry), and the CTP528 (line-pair) Catphan® modules. To identify and remove individual events caused by fragmentation, the multistage energy detector of the scanner was adapted to function as a $\Delta E - E$ telescope.

The use of the developed filter eliminated the otherwise arising ring artifacts in the HeCT reconstructed images. For the HeCT reconstructed images of a water phantom, the maximum RSP error was improved by almost a factor 8 with respect to unfiltered images in the simulation and a factor 10 in the experiment. Similarly, for the CTP404 module, the mean RSP accuracy improved by a factor 6 in both the simulation and the experiment when the filter was applied (mean relative error 0.40% in simulation, 0.45% in experiment). In the evaluation of the spatial resolution through the CTP528 module, the main effect of the filter was noise reduction. For both simulated and experimental images the spatial resolution was ~4lp/cm.

In conclusion, the novel filter developed for secondary fragments proved to be effective in improving the visual quality and RSP accuracy of the reconstructed images. With the filter, the pCT scanner is capable of accurate HeCT imaging.

Keywords

Helium computed tomography; fragmentation; ion imaging; proton imaging; single-event imaging; ion CT detector

1. Introduction

Ion imaging was first proposed conceptually by Cormack (1963) in the form of proton computed tomography (pCT). The first experimentally acquired proton radiography (pRad) was published just a few years later (Koehler 1968). Studies on heavy ion imaging (atomic number $Z > 1$) followed shortly after (cf. Benton et al. (1973)). However, due to the need for large accelerators to produce ions of sufficient energy for imaging, this imaging modality was impractical for diagnostic use. Only with the advent of proton and ion radiotherapy, ion imaging gained increasing interest in the medical community.

Ion radiotherapy makes use of the favorable depth dose profile of ions, the *Bragg peak*, for a highly localized dose deposition in the patient. To maximize the treatment accuracy, knowledge of the position of the Bragg-peak distal fall-off within the patient is crucial. The distance from beam entry to a specified relative dose point on the distal slope of the fall-off (e.g., 90% of the peak dose) which is related to the range of the ions can be obtained from the Bethe-Bloch stopping power formula (Bethe & Ashkin 1953, Doolan et al. 2016). In current clinical practice, the stopping power information within the patient is retrieved by converting Hounsfield Units (HUs) from a X-ray planning CT to relative stopping power (RSP) (Schneider et al. 1996), defined as the stopping power of a material relative to that of water. The conversion from HU to RSP introduces range uncertainties (Yang et al. 2012) which have to be accounted for in clinical treatment planning, for example, by adding a 3.5% plus a 3 mm margin (Paganetti 2012). Dual energy X-ray CT allows a better separation between electron density and atomic number effects on HU than single-energy CT, and should, therefore, improve the range uncertainty associated with the use of X-ray CT in treatment planning (Zhu & Penfold 2016, Bär et al. 2017, Wohlfahrt et al. 2017). This has been evaluated in animal tissues with promising results (Taasti et al. 2017, Möhler et al. 2018, Bär et al. 2018).

Ion imaging, on the other hand, can provide the direct reconstruction of the voxelized RSP information (Zygmanski et al. 2000). Moreover, ion imaging is expected to provide a better signal-to-noise ratio and higher density resolution at a lower dose level compared to conventional X-ray CT (Schulte et al. 2005, Depauw & Seco 2011). Finally, it does not suffer from beam hardening or metal artifacts (Depauw & Seco 2011, Ordoñez et al. 2017).

However, the spatial resolution of ion imaging suffers from multiple Coulomb scattering (MCS) which leads to non-linear ion trajectories. In single-event ion imaging this problem is addressed by the individual reconstruction of each ion path through the object. Various path

estimation techniques have been developed among which the most likely path (MLP) algorithm is the most commonly used (Williams 2004, Li et al. 2006, Schulte et al. 2008, Erdelyi 2009, Collins-Fekete et al. 2017b). The MLP algorithm requires the knowledge of position and direction before and after the object of each projectile particle, as well as its residual energy. Therefore, ion imaging requires sophisticated detector systems, capable of measuring particle track information and residual energy/range on a single-event basis (Schulte et al. 2008). To date, several different prototype systems have been developed (Bashkirov et al. 2009, Seco & Depauw 2011, Talamonti et al. 2012, Uzunyan et al. 2015, Bashkirov et al. 2016a, Price 2016, Pettersen et al. 2017, Gehrke et al. 2017).

Additionally, current investigations in the field of single-event ion imaging focus on the choice of the optimal ion species to generate images. Whereas until now most studies have been based on protons, recently helium ions were identified to have a great potential especially in terms of spatial resolution (Hansen et al. 2014, Collins-Fekete et al. 2017b, Gehrke et al. 2018, Piersimoni et al. 2018).

In 2016, a collaboration between the German Cancer Research Center (DKFZ) and the U.S. pCT consortium‡ was established to investigate helium single-event radiography (HeRad) and tomography (HeCT). The U.S. pCT consortium prototype scanner (Bashkirov et al. 2016b, Johnson et al. 2016) that is capable of high quality pCT imaging (Plautz et al. 2016, Giacometti et al. 2017, Piersimoni et al. 2017, Johnson et al. 2017) was tested for the operation with helium beams at the Heidelberg Ion-Beam Therapy Center (HIT). However, while preliminary results reported in Volz et al. (2017) and Collins-Fekete et al. (2017a) confirmed the expected increase in spatial resolution between pRad and HeRad, ring artifacts and a relatively low RSP accuracy were present for HeCT. This may be attributed to the projectile fragmentation processes of helium ions that are not present for protons. Fragments, both arriving from the object and generated inside the detector, have to be carefully identified and separated from the primary particle histories for accurate image reconstruction.

In this work, the effect of fragments in helium ion imaging with the pCT consortium prototype both in Monte Carlo (MC) simulation and experiment was investigated. A filtering method was developed using the multistage design of the pCT scanner energy/range detector as a $\Delta E - E$ telescope to efficiently remove all secondary particles before image reconstruction.

2. Theory

2.1. Fragmentation Processes for Helium Ions

In traversing the object and the detector material ions can undergo nuclear interactions with the target nuclei. Both elastic nuclear interactions and mass/charge changing inelastic interactions are possible, the latter resulting in the production of secondary particles.

‡Here, U.S. pCT consortium refers to the collaboration of Loma Linda University (LLU), University of California at Santa Cruz (UCSC) and California State University San Bernardino (CSUSB) (http://scipp.ucsc.edu/pCT/index.html).

Secondary particles from nuclear interactions can be grouped into “target” and “projectile” fragments. Target fragments can have a large atomic number, but are usually produced with only a small energy/range (Loveland et al. 1986, Zeitlin & La Tessa 2016) and, therefore, have no significant impact on ion imaging other than depositing unwanted dose to the object. Projectile fragments, on the other hand, are lower charge/mass remnants of primary ions that underwent nuclear break up in collision with a target nucleus. They usually undergo only a minor change of velocity and direction relative to the original projectile (Goldhaber 1974, Wilson 1983, Morrissey 1989, Morrissey 1993, Zeitlin & La Tessa 2016, Rovituso et al. 2017). Helium ions, due to the especially strong bond of the helium nucleus, are less likely to fragment compared to heavier ions (Cucinotta et al. 1993, Mairani et al. 2016, Zeitlin & La Tessa 2016, Rovituso et al. 2017) and have only six fragmentation channels producing neutrons, protons (p), deuterons (d), tritons (t) and ^{3}He. The predominantly produced helium fragments are protons that have essentially the same residual range as the primary helium ions (Rovituso et al. 2017). The produced charged fragments are detected in ion imaging systems with single-event registration, but are not readily distinguished, leading to a mixing of the energy loss of primaries and the lower energy deposit of fragments. An effective filter of secondary fragments is, therefore, crucial for accurate helium ion imaging.

2.2. The ΔE − E Technique

The general principle of a conventional $\Delta E{-}E$ telescope is to measure the energy loss in a thin absorber (ΔE) and the total residual energy (E) in a thick absorber immediately following the thin absorber for each projectile particle crossing the system. Following the formalism by Tassan-Got (2002) for a particle with atomic number Z, atomic mass A and total kinetic energy $\mathscr{E} = E + \Delta E$, the Bethe-Bloch stopping power can be written in a simplified way as:

$$\frac{\mathrm{d}\mathscr{E}}{\mathrm{d}x} = \frac{Z^2}{f(\mathscr{E}/A)}. \quad (1)$$

Defining $F(x)$ as $\mathrm{F} := \int_0^x f(t)\mathrm{d}t$, ΔE can be written as a function of E:

$$\Delta E = A\left[F^{-1}\left(F\left(\frac{E}{A}\right) + \frac{Z^2}{A}\Delta X\right) - \frac{E}{A}\right], \quad (2)$$

where ΔX is the thickness of a homogeneous ΔE detector. Due to the dependence on Z and A in equation 2, plotting E against ΔE for each event results in separated response curves for different particle species, consequently enabling particle identification in a mixed beam (Carboni et al. 2012).

3. Materials and Methods

3.1. The Prototype Scanner

For this study the prototype scanner built by the U.S. pCT consortium was used. The prototype was originally developed for proton beams and its design and operation have been described already elsewhere (Sadrozinski et al. 2013,Bashkirov et al. 2016b, Bashkirov et al. 2016a, Sadrozinski et al. 2016, Johnson et al. 2016, Johnson et al. 2017). Figure 1 shows the scanner installed at the HIT experimental beam line.

The residual energy/range of each particle is measured with a custom-designed 5-stage energy/range detector (Bashkirov et al. 2016b). Each stage is made of plastic scintillating material (polystyrene UPS-923A) and has a dimension of 375 × 100 × 50.8mm^3. The scintillation light is collected by Hamamatsu R3318 photomultiplier tubes (PMTs) and converted into digital values by custom readout electronics (Johnson et al. 2016). The scanner is able to resolve particle rates up to 1MHz with less than 5% event pile up for the setup investigated in Giacometti et al. (2017) and a data acquisition dead time of less than 4%. More details of the operation principle and performance of the scanner have been previously presented in Bashkirov et al. (2016a).

3.2. Calibration

Before the scanning experiment, the response of the energy/range detector was calibrated to water equivalent path length (WEPL) using a dedicated polystyrene object of known water equivalent thickness. The calibration procedure was originally developed by Bashkirov et al. (2016a). For the present work, the recently refined calibration procedure as given in Piersimoni et al. (2017) and Piersimoni et al. (2018) was followed. Two polystyrene wedges (120 × 120 × 50.8mm^3) and 4 polystyrene degraders (280 × 120 × 50.8mm^3) were used. The calibration was reproduced also in the simulations. The polystyrene material had a RSP= 1.030 ± 0.003 for the experimental, and a RSP=1.043 for the simulated setup (Piersimoni et al. 2017, Piersimoni et al. 2018).

3.3. Simulation

MC simulations were performed using the simulation toolkit TOPAS (Perl et al. 2012) release 2.0 patch 3 with Geant4 (Agostinelli et al. 2003, Allison et al. 2006, Allison et al. 2016) version 10.01 patch 02. The default physics list was activated for the TOPAS application. This so-called “Modular Physics List” considers both electromagnetic and nuclear processes relevant for ion therapy (Testa et al. 2013). In detail, it comprises the following Geant4 physics lists: G4EmStandardPhysics_option4 for the most accurate electromagnetic interaction models available in standard and low energy categories,G4HadronPhysicsQGSP_BIC_HP,G4DecayPhysics, IonBinaryCascadePhysics and G4HadronElasticPhysicsHP for modeling nuclear interactions, and G4StoppingPhysics for nuclear capture at rest.

The simulated detector geometry presented in Piersimoni et al. (2017) was used for this work as well. A flat, ideal beam source was used for the simulations irradiating a 200 × 100mm^2 field for phantom studies and 360 × 90mm^2 for the calibration setups. Primary

helium ions were simulated with an initial energy of 200MeV/u. For each projection $2{\cdot}10^6$ particles were used. A full tomographic scan consisted of 90 projections at a 4° angular step, following the work-flow established by Plautz et al. (2016).

3.4. Experimental Setup at the Heidelberg Ion-Beam Therapy Center

Experiments were conducted at the HIT facility operating the U.S. pCT consortium scanner with helium beams.

The helium ion beams were delivered through the beam monitoring nozzle at the HIT beam line dedicated to experiments (Haberer et al. 2004). A $200 \times 100\text{mm}^2$ field was irradiated using the HIT raster scanning with a spot size of 10.2mm FWHM. The beam initial energy was set to 200.38MeV/u (261.8mm range in water). The particle rate was set to ~ 800kHz to avoid event pile-up. Full tomographic scans were acquired in 90 individual projections in steps of 4°. Each projection consisted of $\sim 2.5 \cdot 10^6$ particles. For each calibration run $\sim 5 \cdot 10^6$ particles were used.

3.5. Investigated Phantoms

A cylindrical water phantom of 150mm diameter and 40mm height was investigated to disentangle the effect of fragments on HeCT from effects originating from the phantom geometry. The phantom container is made of a hollow plastic cylinder with 6.35mm shell thickness that is filled with purified and degasified water (G4_WATER in simulation) and sealed by 6.35mm thick plastic top and bottom plates.

The Catphan ®QA modules (The Phantom Laboratory, Norfolk, Virginia, USA) were HeCT scanned in both simulation and experiment in order to analyze the impact of secondaries on RSP accuracy and spatial resolution. For the simulation, digital versions of both phantoms were based on the implementation by Giacometti et al. (2017).

In detail, the CTP404 sensitometry module was used to evaluate the RSP reconstruction accuracy. The phantom is an epoxy cylinder of 150mm diameter and 25mm height. It contains six tube inserts (12.2mm diameter) of different plastic materials. The RSP in the center of each material insert was measured in a circular region of interest (ROI) with a radius of 3mm and averaged over the 5 most central slices. The RSP of the epoxy material was measured at the same radial position as the inserts. The relative error of the reconstructed RSP was calculated by comparison to peakfinder (PTW, Freiburg, Germany) measurements (Giacometti et al. 2017) for the experiment, and to the RSP calculated directly from the implemented material compositions in the simulation.

The CTP528 high resolution module was used to evaluate the spatial resolution of the acquired HeCT images. The phantom is a cylinder (40mm height, 150mm diameter) made of the same epoxy material as the CTP404 and containing aluminum line-pair inserts with increasing spatial frequency (1 – 21lp/cm). The modulation transfer function (MTF) was calculated by comparing the maximum-to-minimum contrast at each line pair insert to the reference contrast:

$$MTF(x) = \frac{\langle \mathrm{RSP}_{max} - \mathrm{RSP}_{min} \rangle}{\mathrm{RSP}_{Al} - \mathrm{RSP}_{Epoxy}}, x \in \{1\mathrm{p/cm}, \ldots, 21\mathrm{p/cm}\} . \quad (3)$$

The RSP of aluminum is 2.11, that of the Epoxy material 1.14 (Giacometti et al. 2017). The $MTF_{10\%}$, defined as the number of line pairs per cm resolved at 10% of the contrast, was used to quantify the spatial resolution (Seco et al. 2013).

3.6. The Energy/Range Detector as a ΔE − E Telescope

The 5-stage structure of the energy detector was adapted to be used as a $\Delta E - E$ telescope. The concept is explained schematically in figure 2. The energy deposit measured in the stage where the ion stops (henceforth denoted *Bragg-peak stage*) was used as the residual energy E. ΔE was then defined as the energy deposited for the same event in the stage adjacent to the Bragg-peak stage in upstream direction (noted as ΔE *stage*).

For each stage (except stage 1) the $\Delta E - E$ spectrum was plotted using the detector response from the 5 calibration runs. In the simulation, the response curves were then identified by plotting the spectrum of each fragment species individually. In experiment, the individual response curves in the $\Delta E - E$ spectrum were identified by comparison with the simulation. The primary helium curve was parametrized with a second degree polynomial function which could subsequently be used as a filter for secondary fragments in the pre-processing of the image data.

3.7. Pre-Processing and Image Reconstruction

Image reconstructions were performed using 3 different pre-processing modalities: using all events without filtering secondary fragments, applying a standard threshold filter on the energy loss in each stage prior to the Bragg-peak stage, and applying the $\Delta E - E$ filter specifically developed.

The standard threshold filter removed all events with energy deposition lower than the lower bound energy deposit in each stage prior to the Bragg-peak stage based on a simulated helium depth dose curve when no phantom was placed in the beam line (within 5σ deviation). The same threshold filter has also been used for proton imaging with the device.

The $\Delta E - E$ filter was based on comparing the relationship between the energy deposit in the Bragg-peak stage of an event and the respective ΔE stage to the parameterization of the helium response curve derived for these stages during the calibration. The events for which the $\Delta E - E$ relationship was not compatible with the parameterized helium curve within a certain margin based on the relative occurrence frequency (see figure 4) were discarded for the image reconstruction.

Before the image reconstruction, also a 3σ cut was applied to the angular displacement and WEPL to filter out large angle scattering and unusually large energy losses for all setups.

The particle trajectories were estimated using the MLP algorithm by Schulte et al. (2008) that was recently shown to be also applicable for helium ions (Collins-Fekete et al. 2017b). Images were reconstructed using the diagonally relaxed orthogonal projection (DROP) iterative reconstruction technique with superiorization of the total variation norm (TVS), here denoted as DROP-TVS algorithm (Penfold et al. 2010). The Feldkamp-David-Kress (FDK) algorithm was used to generate the starting iteration for the algorithm (Giacometti et al. 2017) and to perform a hull projection as described in Schultze et al. (2015). The DROP-TVS algorithm was run for 8 iterations and using 40 reconstruction blocks to allow a comparison with the experimental pCT results presented in Giacometti et al. (2017). A recent study (Schultze et al. 2018) showed that a higher number of iterations would increase the spatial resolution and RSP accuracy, but would also enhance noise.

4. Results

4.1. ΔE − E Spectrum of the Detector

Figure 3 shows the individual $\Delta E - E$ spectrum for relevant secondary particles from a simulated calibration run with the 2 wedges and 2 degraders, so that most particles stop in stage 3. The spectrum was acquired by plotting the energy loss in stage 3 of all particles stopping in that stage, against their energy deposit in stage 2. Figures 3(a), (b), (c), (d), (e), and (f) show, respectively, the plots for protons, deuterons, tritons, ^{3}He, secondary and primary ^{4}He. The depicted spectra are overall very similar to the experimental measurements by Rovituso et al. (2017).

With the same setup, the total energy deposited by all particles stopping in stage 3 was plotted against the energy deposited in stage 2, for both simulation (figure 4(a)) and experiment (figure 4(b)). The response curves in the spectra were identified by comparison with figure 3.

The noise visible in the spectra corresponds to particles stopping in stage 3 before reaching the Bragg-peak region due to nuclear interaction or scattering events. Especially noteworthy is the vertical pattern at approximately 110MeV energy deposit in stage 2 visible in both figures 3(f) and figure 4. The pattern is located around an energy deposit in stage 2 expected for ^{4}He primaries that should stop in stage 5 (i.e. having crossed little to no WEPL). Hence, this pattern was likely caused by projectile particles that missed the phantom, but stopped in stage 3 before reaching their Bragg-peak region.

The dashed black line depicts the standard threshold that filters out most of the proton, deuteron and triton contamination, as seen by comparison with figure 3. However, the ^{3}He contamination was not affected by this filter. The margins of the $\Delta E - E$ filter are indicated by the dashed red lines in figure 4. The $\Delta E - E$ filter separated ^{4}He from noise and ^{3}He fragments.

In the experiment, approximately 38% of the events were removed by the $\Delta E - E$ filter compared to the data without filtering fragments for the setup investigated here. In simulation, this number was slightly higher with ~ 43% of events cut.

Notably, the experimentally acquired and simulated spectra in figure 4 differ from each other. This effect will be discussed in more detail in section 5.2.

4.2. HeCT Reconstructed Images of the Water Phantom

Figure 5 shows HeCT reconstructed images of the water phantom. In figures 5(a), 5(b), and 5(c), are shown, respectively, an experimentally acquired HeCT reconstructed image with no filtering of secondaries, a reconstructed image with the standard threshold filter, and a reconstructed image with the $\Delta E{-}E$ filter applied. Figure 5(d) shows a simulated HeCT reconstructed image with the $\Delta E - E$ filter for comparison. Strong ring artifacts are visible for the reconstructions of the unfiltered and the threshold filtered events.

Transverse profiles along the lines in figure 5 through the HeCT reconstructed images are shown in figure 6(a) and figure 6(b) for simulated and experimental data, respectively. The ring artifacts visible in figure 5(a) and (b) are reflected by significant fluctuations in the profiles of the unfiltered and threshold filtered HeCT reconstructed images. For the unfiltered HeCT, edge effects were present at the radial position of the phantom plastic shell. In the center, the ring artifacts in the unfiltered HeCT resulted in fluctuations above 4% compared to the mean value for the simulation, and above 6.5% for the experiment. With the threshold filter, the ring artifacts were only slightly reduced and still resulted in deviations of ~ 4% from the mean for the simulation, and ~ 6% for the experiment. With the $\Delta E{-}E$ filter fluctuations in the HeCT reconstructed images of the simulated data were reduced to less than 0.2% with respect to the mean. For the experimental data, the $\Delta E - E$ filtered HeCT reconstructed images presented fluctuations of less than 0.5% with respect to the mean value.

Figure 6(c) and figure 6(d) depict the distribution of the voxelized RSP values in a ROI of 60mm radius in the center of the reconstructions accumulated over the 9 most central slices for simulated and experimental HeCT reconstructed images, respectively. Both in the simulation and the experiment, the RSP values for the unfiltered and threshold filtered HeCT reconstructed images are spread over a range of several percent relative error without following a clear distribution. The maximum relative error was 4.24% for the unfiltered and 4.01% for the threshold filtered HeCT in the simulation. In the experiment, the unfiltered HeCT presented a maximum relative error of 7.83% and the threshold filtered HeCT a maximum of 6.35%. Conversely, with the $\Delta E{-}E$ filter, the reconstructed RSP values followed a sharp distribution. In the simulation, the mean relative RSP error of the $\Delta E{-}E$ filtered HeCT reconstructed images was $(0.24 \pm 0.07)\%$. In the experiment, the mean relative error was $(0.15{\pm}0.22)\%$. The experimental distribution was broader compared to the simulated and presented a shoulder for smaller RSP values.

4.3. Relative Stopping Power Accuracy

Figure 7 depicts 4 HeCT reconstructions of the CTP404 sensitometry module with different settings. In figure 7(a)-(c) experimental data are reported, while figure 7(d) shows the simulated HeCT for comparison. Figure 7(a) and 7(b) show, respectively, an unfiltered HeCT reconstructed image and one with the standard threshold filter applied. Figure 7(b) appears similarly in a previous publication (Volz et al. 2017). Figures 7(c) and 7(d) show

reconstructed HeCT images using the $\Delta E - E$ filter for an experimental and a simulated scan, respectively. The images were reconstructed using 256×256 pixels per slice (0.7mm pixel size) and a slice thickness of 2.5mm similar to treatment planning voxel sizes.

Again, ring artifacts visible in figures 7(a) and 7(b) were not present for the $\Delta E{-}E$ filtered images. As is indicated by the horizontal lines in the images on figure 7, traverse profiles along a diameter through each pair of opposing material inserts were plotted and are shown in figure 8. Similarly to the reconstructions of the water phantom, the unfiltered HeCT of the CTP404 module yielded strong edge effects. The threshold filter reduced the artifacts, particularly on the edge of the phantom, while in the center the unfiltered and threshold filtered images showed a similar trend. The fluctuations in the profile were greatly reduced when the $\Delta E - E$ filter was applied. Simulated and experimental reconstructions with the new filter were similarly smooth. The small deviations between the experimental and simulated RSP values for the inserts stemmed from a slight difference in the simulated compared to the real material composition.

The RSP accuracy of the HeCT reconstructed images was evaluated and compared to reference values (peakfinder measurements for experiment, calculated values from the implemented material composition for simulation). The mean relative error of the RSP values reconstructed for the plastic inserts and the epoxy material was (2.39 ± 0.58)% for the unfiltered, and (2.90 ± 0.48)% for the threshold filtered experimental HeCT, where the given error is the standard error of the mean. Moreover, the RSP values for both the unfiltered and threshold filtered reconstructions were subject to large noise, resulting in standard deviations of the reconstructed RSP values ranging up to ~ 2%.

When the $\Delta E{-}E$ filter was applied, the mean relative error was (0.40±0.19)% and (0.45 ± 0.22)% for simulated and experimental HeCT, respectively. The relative error and respective standard deviation of the $\Delta E{-}E$ filtered HeCT reconstructed values for each insert are shown in figure 9. For comparison, figure 9 also shows the accuracy of pCT acquired with the system (Giacometti et al. 2017).

In the experiment, the highest relative error was seen for PMP at (0.99±0.43)%. In the simulation, only for LDPE the relative error was above the clinically acceptable limit at (1.01 ± 0.12)%. Similar results have been previously presented for experimentally acquired pCT with the same scanner (mean relative error 0.43%, relative error 1.36% for PMP and 0.81% for LDPE).

4.4. Spatial Resolution

Figure 10(a) and figure 10(b) show, respectively, an experimental and a simulated HeCT transverse slice of the CTP528 module. Ring artifacts, similar to the ones observed for the other phantoms discussed above, were removed by applying the $\Delta E{-}E$ filter. Streak artifacts in the center of the reconstructions are visible. The MTF of the system was evaluated using the aluminum line pairs and the result is shown in figure 11. A sigmoid fit was performed to yield the MTF over the whole spatial frequency range (Seco et al. 2013).

The MTF of both the simulated and experimentally acquired HeCT are very similar, with variations compatible within one standard deviation. The spatial resolution is only slightly lower if secondary fragments are not filtered before reconstruction as shown by the dashed gray line in figure 11. The unfiltered experimental HeCT yields an $MTF_{10\%}$ of 3.7lp/cm. The $MTF_{10\%}$ for the $\Delta E{-}E$ filtered HeCT is 3.8lp/cm in experiment and 3.7lp/cm in simulation.

5. Discussion

5.1. The Effect of Fragments and the ΔE − E Filter

In this study, the effect of secondary fragments on HeCT imaging was investigated both for MC simulation and experiment. The ring artifacts and low RSP accuracy visible in HeCT images acquired with the U.S. pCT consortium prototype scanner (Volz et al. 2017) were shown to be caused by secondary fragments produced inside the the multistage energy/range detector. In general, fragments introduced additional errors to the reconstructed WEPL. The largest errors were seen at stage interfaces of the multistage detector, where fragments can stop in an adjacent stage compared to the primaries.

The effect of fragmentation in single-event helium imaging has been recently investigated for radiography with a CMOS active pixel setup by Gehrke et al. (2017). In that work, a threshold based on the much lower energy deposit of protons compared to primary helium ions was used to filter out fragments, showing an improvement of the image quality. The present work showed that with a similar threshold filter, able to remove most of the proton, deuteron and triton contamination, the HeCT reconstructed images still presented reduced RSP accuracy and significant fluctuations. Conversely, with the $\Delta E - E$ filter which was able to distinguish also ^{3}He fragments images with high RSP accuracy and without large ring artifacts were obtained. Despite the fact that ^{3}He fragments only represented a small percentage of the overall secondary yield, their effect on the reconstruction accuracy was relatively large.

As shown in figures 5 and 6, with the $\Delta E - E$ filter, fluctuations were reduced to less than 0.2% compared to the mean RSP value in simulation, and to less than 0.5% in the experiment. Similar fluctuations have also been observed for pCT with the detector (Piersimoni et al. 2017, Giacometti et al. 2017) and were attributed to the detector calibration procedure rather than secondary fragments. Further improvement of the detector calibration is under investigation.

The $\Delta E - E$ filtered reconstructions of the Catphan CTP404 module yielded a RSP uncertainty better than the clinically acceptable limit of 1% for most inserts. Especially, the $\Delta E - E$ filter improved the mean RSP accuracy by a factor 6 compared to the unfiltered and threshold filtered reconstructions. A comparable RSP accuracy for experimental pCT data to that of the $\Delta E - E$ filtered HeCT is reported in Giacometti et al. (2017).

The MTF evaluated through the line pairs in the CTP528 module was not significantly affected by secondary fragments. Both the simulated and experimentally acquired HeCT images of the CTP528 module yielded similar MTFs with an $MTF_{10\%}$ of ~ 4lp/cm. An

initial energy higher than the 200 MeV/u used in the present study would lead to an increase in spatial resolution due to reduced MCS (Seco et al. 2013), but the contrast-to-noise ratio would be expected to decrease due to the increased energy/range straggling (Schulte et al. 2005, Amato et al. 2018). Additionally, in the relevant energy range, the nuclear fragmentation cross sections for helium ions are energy dependent and increases for kinetic energies above 280MeV/u, see, e.g. figure 6 in Horst et al. (2017). Therefore, in future studies, the optimal initial energy for helium imaging of different body sites should be investigated.

A drawback of the filtering is the loss of approximately 38% of the events in experiment and 43% in simulation compared to the event histories when no filtering of fragments is applied, as calculated for a calibration run with two bricks and the two wedges. The higher number in simulation might be a result from the slight difference in implemented and real density of the degrader material and the uncertainty of the Geant4 physics modeling classes regarding nuclear fragmentation. The latter has been investigated for carbon ions (Böhlen et al. 2010, Dudouet et al. 2014, Bolst et al. 2017) and found to be of the order of tens of percent; similar uncertainties are expected to be present for the simulation of helium beams, but no experimental results are yet available. Both simulated and experimental numbers are comparable to the loss of primaries shown by Rovituso et al. (2017) for helium ions with initial energy of 200MeV crossing 200mm of water. However, Gehrke et al. (2018) and Piersimoni et al. (2018) have shown that the quality of helium imaging would not be affected when the number of events used in reconstruction is reduced to 25% with respect to that used for proton imaging.

For the investigated prototype, the $\Delta E{-}E$ filter could not be applied for particles stopping in the very first energy detector stage. However, for an initial energy of 200MeV/u, primary helium ions stopping in the first detector stage correspond to a WEPL of 21cm or more. Hence, the first stage would only become relevant for relatively thick objects. In order to also filter secondary fragments stopping in the first stage, a rear tracker unit capable to measure energy loss on top of position could be used to function as a thin $\Delta E - E$ stage.

The strength of the $\Delta E - E$ filter lies within its generality. It adds only little computational cost when reconstructing the images. Additionally, to enable the technique, only a longitudinally segmented detector measuring the particles energy loss is necessary alongside the requirement that the particles stop within the detector geometry. Finally, as the relationship given by Eq. 2 is applicable for all charged particles, the method could also be extended to other ion species.

5.2. Detector Performance

As can be noticed comparing figure 4(a) and figure 4(b), the response curves in the $\Delta E - E$ spectra were different for the simulated compared to the experimentally acquired detector response. Moreover, in experiment the acquired $\Delta E - E$ spectra also varied among each pair of adjacent detector stages. This dissimilarity could most likely be attributed to a non-linear stage response at high energy depositions. In experiment, the digitized scintillation light output was converted into a numerical energy value using a calibration run with no phantom in the scanner. This method used only one energy calibration point per stage and thus, a

linear stage response was necessary for a correct conversion of the digitized light output to energy over the whole range of possible energy deposits.

However, individual energy depositions were mapped directly to the known WEPL crossed by the particles in the calibration procedure. For this, the numerical energy value was used only as an index to retrieve a WEPL value from the acquired WEPL versus energy map. Therefore, the correct numerical energy in MeV is not important for accurate WEPL reconstructions as long as the values are consistent and no saturation occurs. This was confirmed by the high RSP accuracy achieved in this work. Still, in follow up studies, the linear region of the stage response should be increased to optimize the detector accuracy for HeCT.

For HeCT, 90 projections for a full scan limited the reconstruction accuracy as can be seen by the streak artifacts visible in the reconstructions shown in figure 10. Considering the Nyquist-Shannon (Shannon 1948) sampling theorem, such streak artifacts were a result of sparse view tomographies and an under-sampled system matrix. This was also shown recently in Piersimoni et al. (2018). This work hence did not reflect the full potential of HeCT. A complete comparison of HeCT and pCT was beyond the scope of this work.

Overall, considering the achieved quality of HeCT reconstructed images in this work, the prototype proton detector could be operated with helium beams without altering the design. As the above filter could be adapted for other ion species as well, this renders the pCT consortium prototype design a powerful tool for ion imaging in general.

6. Conclusions

In this work, the effect of projectile fragments on the image reconstruction in ion imaging with a prototype detector was presented. By adapting the $\Delta E - E$ technique to the image reconstruction, a method to filter out secondaries in ion CT imaging was developed. As shown in the HeCT reconstructions presented in this work, applying this filtering resulted in a notable improvement of the image quality both in simulation and experiment, removing almost completely the strong ring artifacts otherwise arising. This can be considered a general result, since secondary fragments can affect the WEPL evaluation in any particle CT scanner system, independent of the detector design.

The developed $\Delta E - E$ method could be applied for imaging with other ion species, or different detector setups as long as the energy detector is longitudinally segmented. The promising spatial resolution and high RSP accuracy achieved both in simulation and experiment affirm the opportunity of further investigating helium ions in single-event imaging, possibly using a larger number of projection angles, to fully exploit the potential of HeCT.

In conclusion, the U.S. pCT consortium prototype pCT scanner was proven to produce high quality HeCT images, when a filter on secondary fragments, in particular, ^{3}He fragments, is applied. Future investigations will therefore focus on identifying/designing the ideal scanner for helium imaging, possibly with an energy detector optimized for helium ions. Under such

conditions, a full comparison of HeCT, pCT, and X-ray imaging modalities could be possible.

Acknowledgments

The authors want to acknowledge the Heidelberg Ion-Beam Therapy Center (HIT) for providing beam time as well as the HIT engineers for their excellent help in planning and conducting the experiments. The authors want to thank Bruce Faddegon and José Ramos-Mendéz for helping with the TOPAS simulations and providing server time. This work was partially supported by grants from the National Institute of Biomedical Imaging and Engineering and the National Science Foundation (NSF) (R01EB013118), the National Cancer Institute (NCI) (1P20183640-A101), and the United States - Israel Binational Science Foundation (BSF) (2009012 and 2013003).

References

Agostinelli S, Allison J, Amako K, Apostolakis J, Araujo H et al. (2003). Geant4—a simulation toolkit, Nuclear Instruments and Methods in Physics Research Section A: Accelerators, Spectrometers, Detectors and Associated Equipment 506(3): 250–303.

Allison J, Amako K, Apostolakis J, Araujo H, Dubois PA et al. (2006). Geant4 developments and applications, IEEE Transactions on Nuclear Science 53(1): 270–278.

Allison J, Amako K, Apostolakis J, Arce P, Asai M et al. (2016). Recent developments in geant4, Nuclear Instruments and Methods in Physics Research Section A: Accelerators, Spectrometers, Detectors and Associated Equipment 835: 186–225. URL: http://www.sciencedirect.com/science/article/pii/S0168900216306957

Amato C, Gehrke T & Martisikova M (2018). Spatial resolution improvements in heliumbeam radiography, Presented at the proton imaging workshop Lyon 2018 **URL**: https://protonimaging.sciencesconf.org/214291**URL**

Bär E, Lalonde A, Royle G, Lu H-M & Bouchard H (2017). The potential of dual-energy ct to reduce proton beam range uncertainties, Medical Physics 44(6): 2332–2344. **URL**: 10.1002/mp.12215</italic></underline> [PubMed: 28295434] **URL**

Bär E, Lalonde A, Zhang R, Jee K, Yang K, Sharp G, Liu B, Royle G, Bouchard H & Lu H (2018). Experimental validation of two dual-energy ct methods for proton therapy using heterogeneous tissue samples, Medical Physics 45(1): 48–59. **URL**: https://aapm.onlinelibrary.wiley.com/doi/abs/10.1002/mp.12666 [PubMed: 29134674] **URL**

Bashkirov VA, Johnson RP, Sadrozinski HF-W & Schulte RW (2016a). Development of proton computed tomography detectors for applications in hadron therapy, Nuclear Instruments & Methods in Physics Research. Section A, Accelerators, Spectrometers, Detectors and Associated Equipment 809: 120–129.

Bashkirov VA, Schulte RW, Hurley RF, Johnson RP, Sadrozinski HF-W, Zatserklyaniy A, Plautz T & Giacometti V (2016b). Novel scintillation detector design and performance for proton radiography and computed tomography, Medical Physics 43(2): 664–674. **URL**: 10.1118/1.4939255</italic></underline> [PubMed: 26843230] **URL**

Bashkirov V, Schulte R, Coutrakon G, Erdelyi B, Wong K, Sadrozinski H, Penfold S, Rosenfeld A, McAllister S & Schubert K (2009). Development of proton computed tomography for applications in proton therapy, Application of accelerators in research and industry: Twentieth International Conference, AIP Conference Proceedings, Vol. 1099, pp. 460–463.

Benton EV, Henke RP & Tobias CA (1973). Heavy-particle radiography, Science 182(4111): 474–476. **URL**: http://science.sciencemag.org/content/182/4111/474 [PubMed: 4744176] **URL**

Bethe HA & Ashkin J (1953). Passage of radiation through matter, John Wiley & Sons; Chapman & Hall, New York; London.

Bolst D, Cirrone GA, Cuttone G, Folger G, Incerti S et al. (2017). Validation of geant4 fragmentation for heavy ion therapy, Nuclear Instruments and Methods in Physics Research Section A: Accelerators, Spectrometers, Detectors and Associated Equipment 869: 68–75.

Böhlen TT, Cerutti F, Dosanjh M, Ferrari A, Gudowska I, Mairani A & Quesada JM (2010). Benchmarking nuclear models of fluka and geant4 for carbon ion therapy, Physics in Medicine &

Biology 55(19): 5833 **URL**: http://stacks.iop.org/0031-9155/55/i=19/a=014 [PubMed: 20844337] **URL**

Carboni S, Barlini S, Bardelli L, Le Neindre N, Bini M et al. (2012). Particle identification using the (DELTA)E-E technique and pulse shape discrimination with the silicon detectors of the FAZIA project, Nuclear Instruments and Methods in Physics Research Section A: Accelerators, Spectrometers, Detectors and Associated Equipment 664: 251–263. **URL**: http://hal.in2p3.fr/in2p3-00656422**URL**

Collins-Fekete C-A, Volz L, Piersimoni P, Ordonez C, Bashkirov V, Coutrakon G, Johnson R, Beaulieu L, Schulte R & Seco J (2017a). We-g-605–5: Theoretical prediction and experimental verification of the spatial resolution and stopping power accuracy of ion radiography/tomography, American Association of Physics in Medicine. URL: https://www.aapm.org/meetings/2017AM/PRAbs.asp?mid=127&aid=37717

Collins-Fekete C-A, Volz L, Portillo SKN, Beaulieu L & Seco J (2017b). A theoretical framework to predict the most likely ion path in particle imaging, Physics in Medicine and Biology 62(5): 1777. [PubMed: 28076336]

Cormack AM (1963). Representation of a Function by Its Line Integrals, with Some Radiological Applications, Journal of Applied Physics 34(9): 2722–2727.

Cucinotta FA, Townsend LW & Wilson JW (1993). Description of alpha-nucleus interaction cross sections for cosmic ray shielding studies, NASA Technical Paper 3285. **URL**: https://ntrs.nasa.gov/search.jsp?R=19930017716**URL**

Depauw N & Seco J (2011). Sensitivity study of proton radiography and comparison with kV and MV x-ray imaging using GEANT4 Monte Carlo simulations, Physics in Medicine and Biology 56(8): 2407–2421. [PubMed: 21427482]

Doolan PJ, Collins-Fekete C-A, Dias MF, Ruggieri TA, D'Souza D & Seco J (2016). Inter-comparison of relative stopping power estimation models for proton therapy, Physics in Medicine & Biology 61(22): 8085 **URL**: http://stacks.iop.org/0031-9155/61/i=22/a=8085 [PubMed: 27781999] **URL**

Dudouet J, Cussol D, Durand D & Labalme M (2014). Benchmarking geant4 nuclear models for hadron therapy with 95 mev/nucleon carbon ions, Phys. Rev. C 89: 054616 **URL**: https://link.aps.org/doi/10.1103/PhysRevC.89.054616**URL**

Erdelyi B (2009). A comprehensive study of the most likely path formalism for proton-computed tomography, Physics in Medicine and Biology 54(20): 6095–6122. [PubMed: 19779216]

Gehrke T, Amato C, Berke S & Martišíková M (2018). Theoretical and experimental comparison of proton and helium-beam radiography using silicon pixel detectors, Physics in Medicine & Biology 63(3): 035037 **URL**: http://stacks.iop.org/0031-9155/63/i=3/a=035037 [PubMed: 29311417] **URL**

Gehrke T, Gallas R, Jäkel O & Martišíková M (2017). Proof of principle of heliumbeam radiography using silicon pixel detectors for energy deposition measurement, identification, and tracking of single ions, Medical Physics pp. n/a–n/a. URL: 10.1002/mp.12723

Giacometti V, Bashkirov VA, Piersimoni P, Guatelli S, Plautz TE et al. (2017). Software platform for simulation of a prototype proton ct scanner, Medical Physics 44(3): 1002–1016. **URL**: 10.1002/mp.12107</italic></underline> [PubMed: 28094862] **URL**

Goldhaber A (1974). Statistical models of fragmentation processes, Physics Letters B 53(4): 306–308. **URL**: http://www.sciencedirect.com/science/article/pii/0370269374903888**URL**

Haberer T, Debus J, Eickhoff H, Jäkel O, Schulz-Ertner D & Weber U (2004). The heidelberg ion therapy center, Radiotherapy and Oncology 73: S186–S190. **URL**: 10.1016/</italic></underline><italic>S0167-8140(04)80046-X</italic> [PubMed: 15971340] **URL**

Hansen DC, Bassler N, Sørensen TS & Seco J (2014). The image quality of ion computed tomography at clinical imaging dose levels, Medical Physics 41(11): 111908. [PubMed: 25370641]

Horst F, Schuy C, Weber U, Brinkmann K-T & Zink K (2017). Measurement of chargeand mass-changing cross sections for $^{4}He+^{12}C$ collisions in the energy range 80–220 mev/u for applications in ion beam therapy, Phys. Rev. C 96: 024624 **URL**: https://link.aps.org/doi/10.1103/PhysRevC.96.024624**URL**

Johnson RP, Bashkirov V, Coutrakon G, Giacometti V, Karbasi P, Karonis N, Ordoñez C, Pankuch M, Sadrozinski H-W, Schubert K & Schulte R (2017). Results from a prototype proton-ct head scanner, Physics Procedia 90: 209–214. Conference on the Application of Accelerators in

Research and Industry, CAARI 2016, 30 October – 4 November 2016, Ft. Worth, TX, USA. **URL**: http://www.sciencedirect.com/science/article/pii/S1875389217302195**URL**

Johnson RP, Bashkirov V, DeWitt L, Giacometti V, HURLey RF et al. (2016). A fast experimental scanner for proton ct: Technical performance and first experience with phantom scans, IEEE transactions on nuclear science 63: 52–60. URL: http://www.ncbi.nlm.nih.gov/pmc/articles/PMC4844465/ [PubMed: 27127307]

Koehler AM (1968). Proton radiography., ACE(.**URL**: http://ntrs.nasa.gov/search.jsp?R=19680045916**URL**

Li T, Liang Z, Singanallur JV, Satogata TJ, Williams DC & Schulte RW (2006). Reconstruction for proton computed tomography by tracing proton trajectories: A Monte Carlo study, Medical Physics 33(3): 699. [PubMed: 16878573]

Loveland W, Aleklett K & Seaborg G (1986). Target fragmentation in intermediate energy heavy ion collisions, Nuclear Physics A 447: 101–114. **URL**: http://www.sciencedirect.com/science/article/pii/0375947486906007**URL**

Mairani A, Dokic I, Magro G, Tessonnier T, Kamp F et al. (2016). Biologically optimized helium ion plans: calculation approach and its in vitro validation, Physics in Medicine & Biology 61(11): 4283 **URL**: http://stacks.iop.org/0031-9155/61/i=11/a=4283 [PubMed: 27203864] **URL**

Möhler C, Russ T, Wohlfahrt P, Elter A, Runz A, Richter C & Greilich S (2018). Experimental verification of stopping-power prediction from single- and dual-energy computed tomography in biological tissues, Physics in Medicine & Biology 63(2): 025001 **URL**: http://stacks.iop.org/0031-9155/63/i=2/a=025001 [PubMed: 29239855] **URL**

Morrissey DJ (1989). Systematics of momentum distributions from reactions with relativistic ions, Phys. Rev. C 39: 460–470. **URL**: https://link.aps.org/doi/10.1103/PhysRevC.39.460**URL**

Morrissey DJ (1993). Comment on “fragmentation of gold projectiles with energies of 200980 mev/nucleon. i. experimental method, charge yields, and transverse momenta”, Phys. Rev. C 47: 413–414. **URL**: https://link.aps.org/doi/10.1103/PhysRevC.47.413**URL**

Ordoñez CE, Karonis N, Duffin K, Coutrakon G, Schulte R, Johnson R & Pankuch M (2017). A real-time image reconstruction system for particle treatment planning using proton computed tomography (pct), Physics Procedia 90: 193–199. Conference on the Application of Accelerators in Research and Industry, CAARI 2016, 30 October – 4 November 2016, Ft. Worth, TX, USA. **URL**: http://www.sciencedirect.com/science/article/pii/S1875389217302171**URL**

Paganetti H (2012). Range uncertainties in proton therapy and the role of Monte Carlo simulations, Physics in Medicine and Biology 57(11): R99 **URL**: http://iopscience.iop.org/0031-9155/57/11/R99 [PubMed: 22571913] **URL**

Penfold SN, Schulte RW, Censor Y & Rosenfeld AB (2010). Total variation superiorization schemes in proton computed tomography image reconstruction, Medical Physics 37(11): 5887–5895. [PubMed: 21158301]

Perl J, Shin J, Schumann J, Faddegon B & Paganetti H (2012). TOPAS: an innovative proton Monte Carlo platform for research and clinical applications, Medical Physics 39(11): 6818–6837. [PubMed: 23127075]

Pettersen H, Alme J, Biegun A, van den Brink A, Chaar M et al. (2017). Proton tracking in a high-granularity digital tracking calorimeter for proton ct purposes, Nuclear Instruments and Methods in Physics Research Section A: Accelerators, Spectrometers, Detectors and Associated Equipment 860: 51–61.

Piersimoni P, Faddegon BA, Méndez JR, Schulte RW, Volz L & Seco J (2018). Helium ct: Monte carlo simulation results for an ideal source and detector with comparison to proton ct, Medical Physics 45(7): 3264–3274. **URL**: https://aapm.onlinelibrary.wiley.com/doi/abs/10.1002/mp.12942 [PubMed: 29727481] **URL**

Piersimoni P, Ramos-Méndez J, Geoghegan T, Bashkirov VA, Schulte RW & Faddegon BA (2017). The effect of beam purity and scanner complexity on proton ct accuracy, Medical Physics 44(1): 284–298. **URL**: 10.1002/mp.12013</italic></underline> [PubMed: 28066887] **URL**

Plautz TE, Bashkirov V, Giacometti V, Hurley RF, Johnson RP, Piersimoni P, Sadrozinski HF-W, Schulte RW & Zatserklyaniy A (2016). An evaluation of spatial resolution of a prototype proton ct

scanner, Medical Physics 43(12): 6291–6300. **URL**: 10.1118/1.4966028</italic></underline> [PubMed: 27908179] **URL**

Price T (2016). Pravda: High energy physics towards proton computed tomography, Nuclear Instruments and Methods in Physics Research Section A: Accelerators, Spectrometers, Detectors and Associated Equipment 824: 226–227.

Rovituso M, Schuy C, Weber U, Brons S, Cortés-Giraldo MA et al. (2017). Fragmentation of 120 and 200 mev u^{-1} ^{4}he ions in water and pmma targets, Physics in Medicine & Biology 62(4): 1310 **URL**: http://stacks.iop.org/0031-9155/62/i=4/a=1310 [PubMed: 28114125] **URL**

Sadrozinski HF-W, Geoghegan T, Harvey E, Johnson RP, Plautz TE et al. (2016). Operation of the preclinical head scanner for proton ct, Nucl Instrum Methods Phys Res A 831: 394–399. [pmid]. **URL**: http://www.ncbi.nlm.nih.gov/pmc/articles/PMC5094456/ [PubMed: 27818559] **URL**

Sadrozinski HF-W, Johnson RP, Macafee S, Plumb A, Steinberg D, Zatserklyaniy A, Bashkirov V, Hurley F & Schulte R (2013). Development of a head scanner for proton ct, Nuclear Instruments & Methods in Physics Research. Section A, Accelerators, Spectrometers, Detectors and Associated Equipment 699: 205–210.

Schneider U, Pedroni E & Lomax A (1996). The calibration of CT Hounsfield units for radiotherapy treatment planning, Physics in medicine and biology 41(1): 111. [PubMed: 8685250]

Schulte RW, Bashkirov V, Klock MCL, Li T, Wroe AJ, Evseev I, Williams DC & Satogata T (2005). Density resolution of proton computed tomography, Medical Physics 32(4): 1035–1046. [PubMed: 15895588]

Schulte RW, Penfold SN, Tafas JT & Schubert KE (2008). A maximum likelihood proton path formalism for application in proton computed tomography, Medical Physics 35(11): 4849–4856. [PubMed: 19070218]

Schultze B, Censor Y, Karbasi P, Schubert KE & Schulte RW (2018). An Improved Method of Total Variation Superiorization Applied to Reconstruction in Proton Computed Tomography, ArXiv e-prints. arXiv:1803.01112.

Schultze B, Witt M, Censor Y, Schubert K & Schulte R (2015). Performance of hulldetection algorithms for proton computed tomography reconstruction, in Reich S & Zaslavski A (eds), Infinite Products of Operators and Their Applications, Vol. 636 of Contemporary Mathematics, American Mathematical Society.

Seco J & Depauw N (2011). Proof of principle study of the use of a CMOS active pixel sensor for proton radiography, Medical Physics 38(2): 622–623. **URL**: http://scitation.aip.org.acces.bibl.ulaval.ca/content/aapm/journal/medphys/38/2/10.1118/1.3496327 [PubMed: 21452699] **URL**

Seco J, Oumano M, Depauw N, Dias MF, Teixeira RP & Spadea MF (2013). Characterizing the modulation transfer function (MTF) of proton/carbon radiography using Monte Carlo simulations, Medical Physics 40(9): 091717. [PubMed: 24007150]

Shannon CE (1948). A mathematical theory of communication, Bell System Technical Journal 27(3): 379–423. **URL**: 10.1002/j.1538-73</italic></underline><italic>05.1948.tb01338.x</italic>**URL**

Taasti VT, Michalak GJ, Hansen DC, Deisher AJ, Kruse JJ, Krauss B, Muren LP, Petersen JBB & McCollough CH (2017). Validation of proton stopping power ratio estimation based on dual energy ct using fresh tissue samples, Physics in Medicine & Biology 63(1): 015012 **URL**: http://stacks.iop.org/0031-9155/63/i=1/a=015012 [PubMed: 29057753] **URL**

Talamonti C, Bruzzi M, Bucciolini M, Carpinelli M, Cirrone GAP et al. (2012). Prima proton imaging for clinical application, 2012 IEEE Nuclear Science Symposium and Medical Imaging Conference Record (NSS/MIC), pp. 2218–2221.

Tassan-Got L (2002). A new functional for charge and mass identification in *δ*e-e telescopes, Nuclear Instruments and Methods in Physics Research Section B: Beam Interactions with Materials and Atoms 194(4): 503–512. **URL**: http://www.sciencedirect.com/science/article/pii/S0168583X02009576**URL**

Testa M, Schümann J, Lu H-M, Shin J, Faddegon B, Perl J & Paganetti H (2013). Experimental validation of the topas monte carlo system for passive scattering proton therapy, Med Phys 40(12): 121719 **URL**: http://www.ncbi.nlm.nih.gov/pmc/articles/PMC4109425/ [PubMed: 24320505] **URL**

Uzunyan SA, Blazey G, Boi S, Coutrakon G, Dyshkant A et al. (2015). Development of a proton ct head scanner, 2015 IEEE Nuclear Science Symposium and Medical Imaging Conference (NSS/MIC), pp. 1–2.

Volz L, Collins-Fekete C-A, Piersimonii P, Johnson RP, Bashkirov V, Schulte R & Seco J (2017). Stopping power accuracy and spatial resolution of helium ion imaging using a prototype particle ct detector system, Current Directions in Biomedical Engineering 3(2): 401–404.

Williams DC (2004). The most likely path of an energetic charged particle through a uniform medium, Physics in Medicine and Biology 49(13): 2899. [PubMed: 15285255]

Wilson JW (1983). Heavy ion transport in the straight ahead approximation, NASA Technical Paper 2178. **URL**: https://ntrs.nasa.gov/search.jsp?R=19830020898**URL**

Wohlfahrt P, Möhler C, Stützer K, Greilich S & Richter C (2017). Dual-energy ct based proton range prediction in head and pelvic tumor patients, Radiotherapy and Oncology 125(3): 526–533. URL: http://www.sciencedirect.com/science/article/pii/S0167814017326282 [PubMed: 29050953]

Yang M, Zhu XR, Park PC, Titt U, Mohan R, Virshup G, Clayton JE & Dong L (2012). Comprehensive analysis of proton range uncertainties related to patient stoppingpower-ratio estimation using the stoichiometric calibration, Physics in Medicine and Biology 57(13): 4095–4115. [PubMed: 22678123]

Zeitlin C & La Tessa C (2016). The role of nuclear fragmentation in particle therapy and space radiation protection, Frontiers in Oncology 6: 65 **URL**: https://www.frontiersin.org/article/10.3389/fonc.2016.00065 [PubMed: 27065350] **URL**

Zhu J & Penfold SN (2016). Review of 3d image data calibration for heterogeneity correction in proton therapy treatment planning, Australasian Physical & Engineering Sciences in Medicine 39(2): 379–390. **URL**: 10.1007/s13246-016-0447-9</italic></underline> [PubMed: 27115163] **URL**

Zygmanski P, Gall KP, Rabin MSZ & Rosenthal SJ (2000). The measurement of proton stopping power using proton-cone-beam computed tomography, Physics in Medicine and Biology 45(2): 511. [PubMed: 10701518]

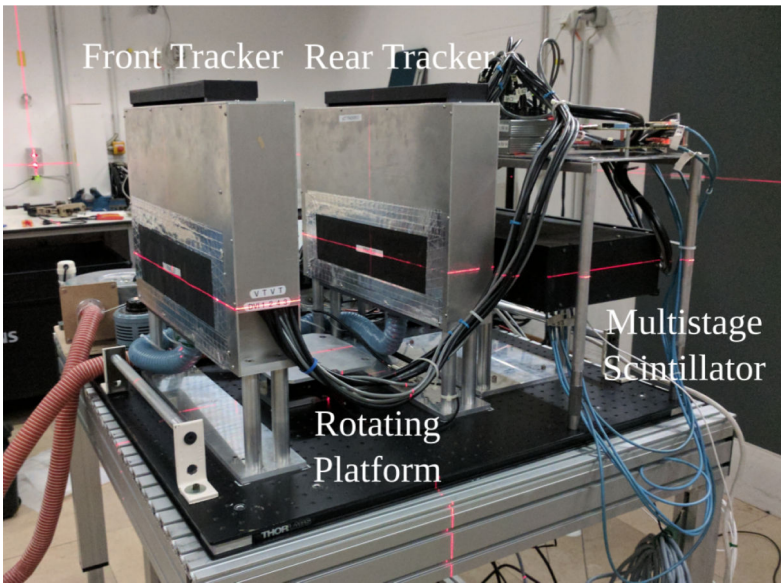

Figure 1.
The U.S. pCT consortium prototype pCT scanner installed at the HIT facility. The detector consists of two tracking detectors, a multistage energy/range detector and a custom high-speed data acquisition board. For the prototype, a rotating platform enables full CT scans of various phantoms.

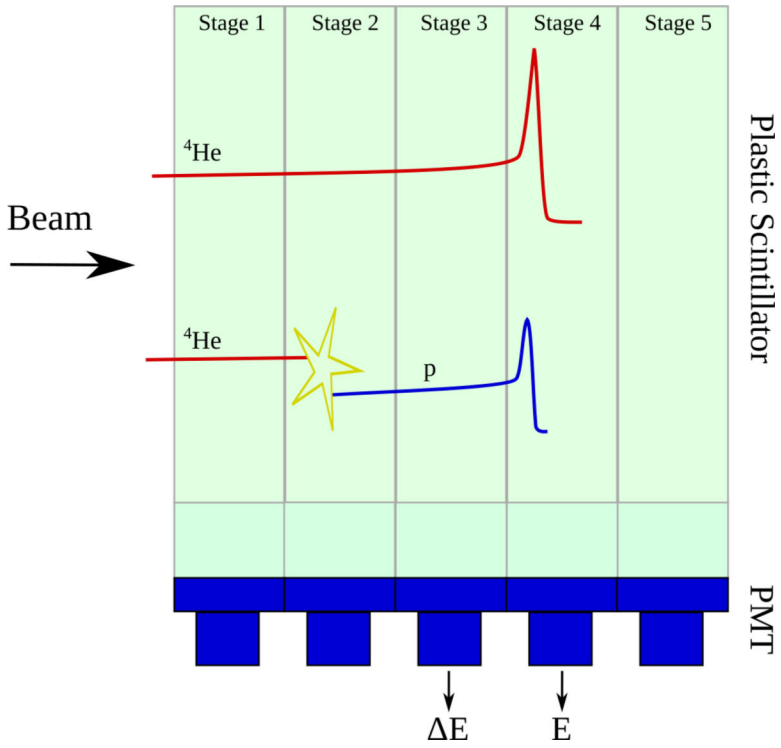

Figure 2.

Drawing explaining how the Δ*E*–*E* technique was used with the U.S. pCT consortium prototype scanner. For each event, the residual energy *E* was taken as the energy deposit in the stage where the particle stopped, while Δ*E* was the energy deposited in the adjacent stage in upstream direction. Helium primaries and secondary fragments stemming from the object to be imaged or from nuclear interactions inside the detector geometry (as depicted by the yellow star) were distinguished by their individual correlation between *E* and Δ*E*.

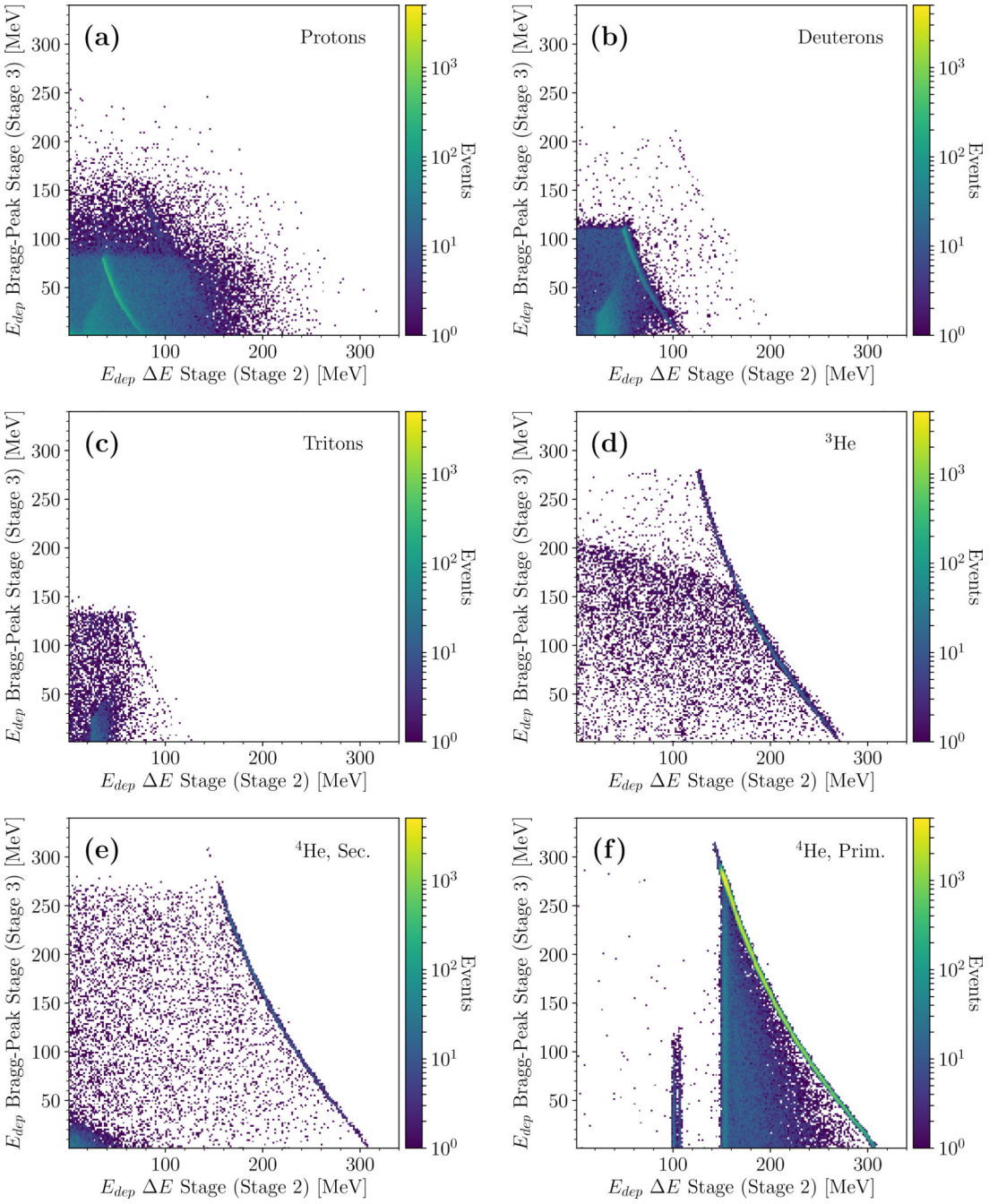

Figure 3.

Simulated $\Delta E - E$ spectrum acquired for a calibration run with the two polystyrene wedges and two polystyrene degraders in the scanner. The energy loss of particles stopping in stage 3 (Bragg-peak stage) was plotted against their respective energy loss in stage 2 (ΔE stage). The plots refer to different particles, as indicated.

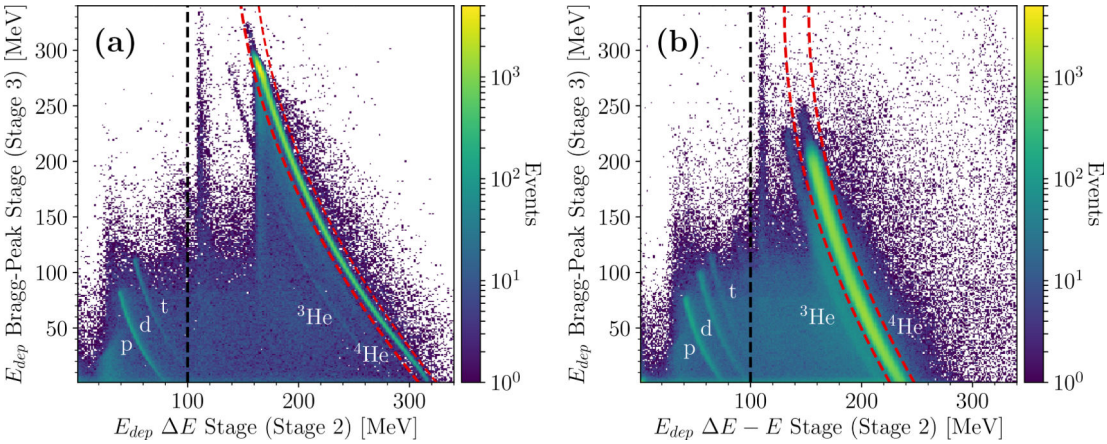

Figure 4.

$\Delta E - E$ spectrum acquired for a calibration run with the two polystyrene wedges and two polystyrene degraders in the scanner. The plot was acquired following the procedure in figure 3 for (**a**) TOPAS simulated data, and (**b**) experimental data. The labels indicate the response curves of individual fragments as found through comparison with figure 3. The dashed red lines and the dashed black line are the ΔE–E filter and the threshold filter, respectively.

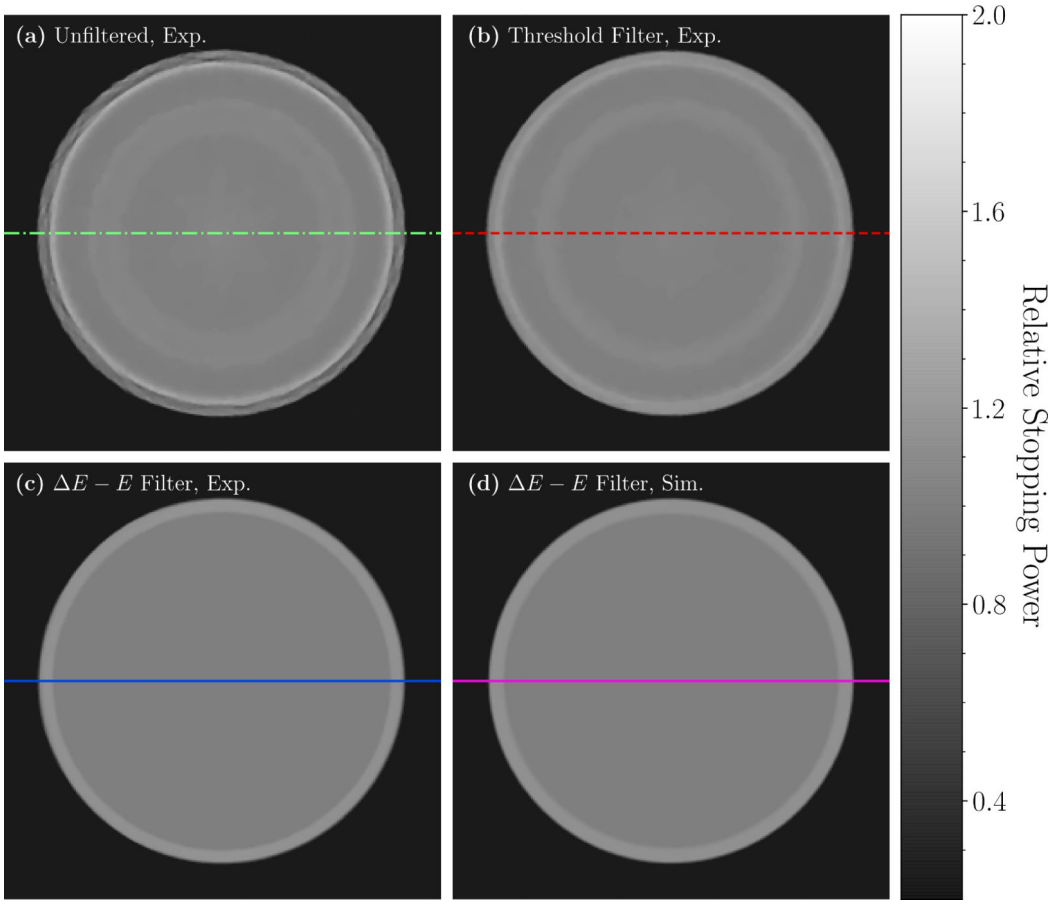

Figure 5.

Transverse slice of the HeCT reconstructed images of the water cylinder. (**a**) Experimental data without filtering of secondaries. (b) Same slice with application of the standard threshold filter. (**c**) Same slice with the new $\Delta E - E$ filter. (**d**) Simulated data with the $\Delta E - E$ filter for comparison. All images were reconstructed with 256×256 pixel per slice (0.7mm pixel size) and slice thickness of 2.5mm.

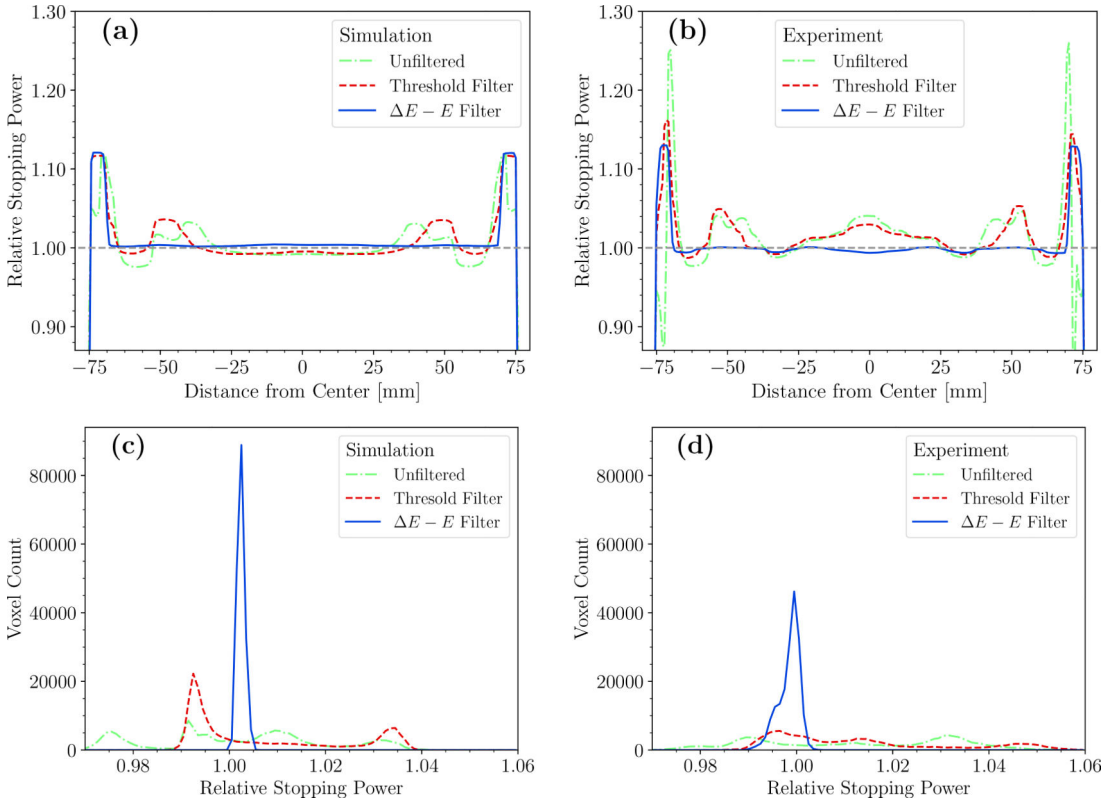

Figure 6.

Quantitative analysis of the simulated and experimental HeCTs of the water cylinder reconstructed with different settings. (**a**) - (**b**) Traverse profiles along a diameter through the simulated and experimental HeCT reconstructed images, respectively. (**c**) - (**d**) Distribution of the reconstructed RSP values in a cylindrical ROI (radius 60mm) in the center of the HeCT reconstructed images for simulated and experimental HeCT, respectively. The dashed green line refers to the reconstruction without filter on fragments, the dashed red line to the reconstruction where a threshold filter was applied, and the solid blue line the reconstruction with the $\Delta E - E$ filter.

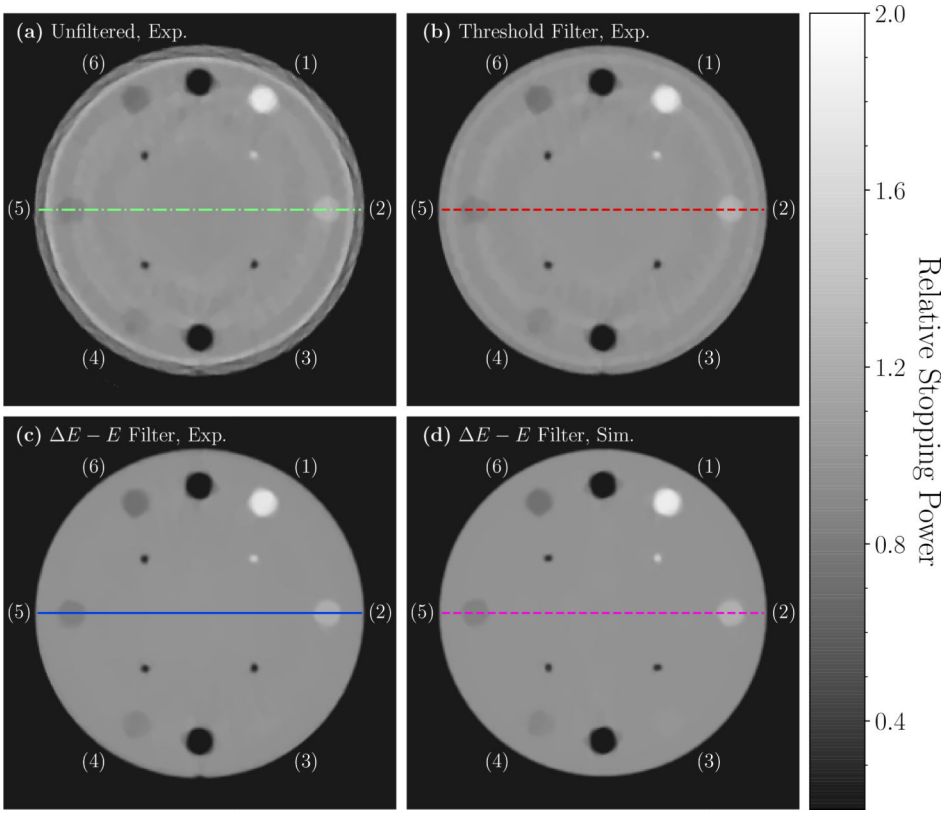

Figure 7.

Experimental HeCT transverse slices of the CTP404 sensitometry module reconstructed with: (**a**) no filtering of secondary fragments; (**b**) standard threshold filter; (**c**) the developed $\Delta E - E$ filter. (**d**) Transverse slice of a simulated HeCT scan for the same phantom reconstructed applying the $\Delta E - E$ filter for comparison. The images were reconstructed with 256×256 pixels per slice (0.7mm pixel size) and slice thickness of 2.5mm. The insert materials are (1) Teflon, (2) delrin, (3) PMMA, (4) polystyrene, (5) LDPE and (6) PMP.

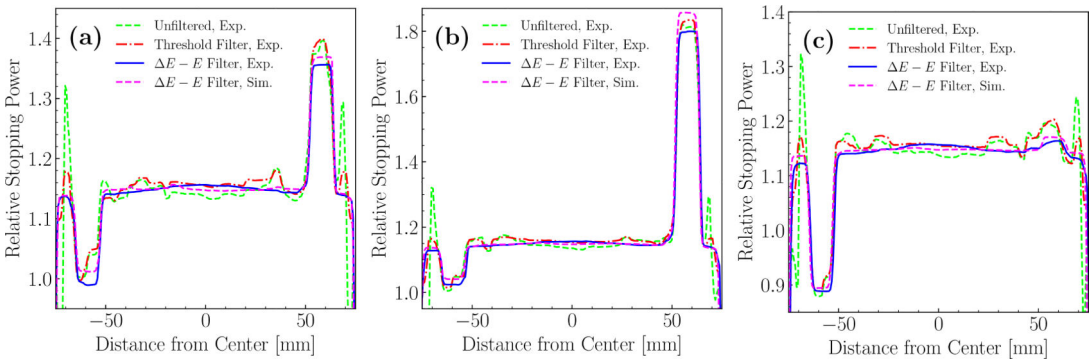

Figure 8.

Traverse profiles through each pair of opposing inserts in the HeCT of the CTP404 module as indicated for LDPE and delrin (**a**) by the horizontal lines in figure 7. Similarly, the profiles were plotted for (**b**) polystyrene and Teflon, and (**c**) PMP and PMMA. The red dashed line refers to the experimental HeCT without filter of fragments, the dashed green line with the standard threshold filter, and the solid blue line with the $\Delta E - E$ filter. The dashed magenta line corresponds to the $\Delta E - E$ filtered simulated HeCT.

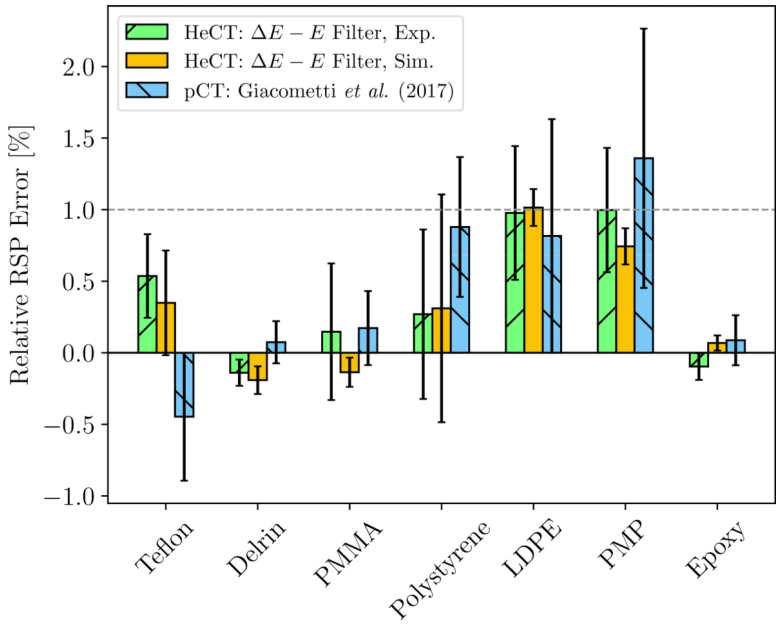

Figure 9.

Relative error of the reconstructed RSP values for the material inserts of the CTP404 sensitometry module and the epoxy material. The dashed green bars are the experimental, the yellow bars the TOPAS simulated reconstruction. For both the $\Delta E - E$ filter was applied. The dashed blue bars are experimental pCT data acquired with the same detector (Giacometti et al. 2017).

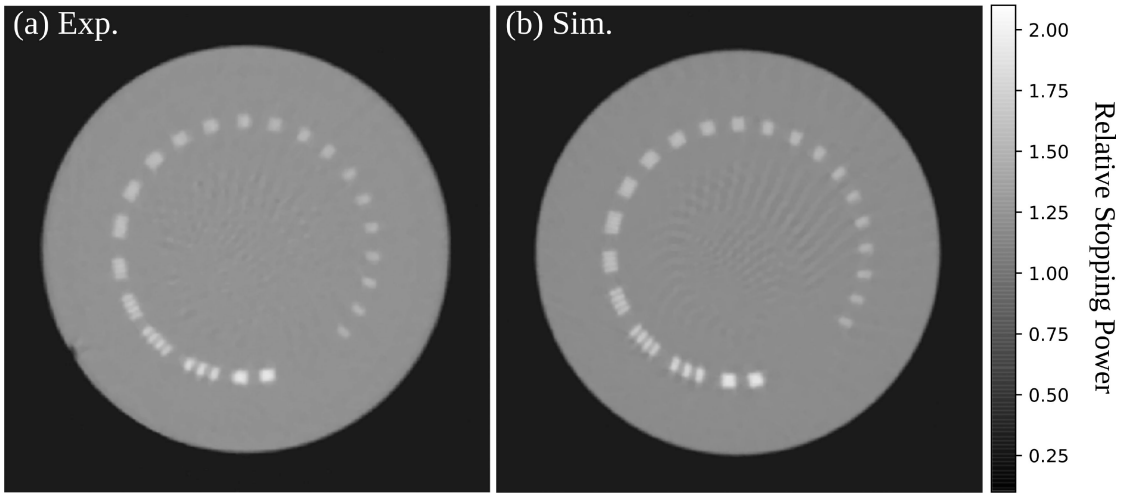

Figure 10.

Traverse slice of the HeCT reconstruction for the CTP528 module where the $\Delta E - E$ filter was applied before image reconstruction. (**a**) Experimental, (**b**) simulated data. The images were reconstructed with 512×512 pixels per slice (0.35mm pixel size) and 1.25mm slice thickness.

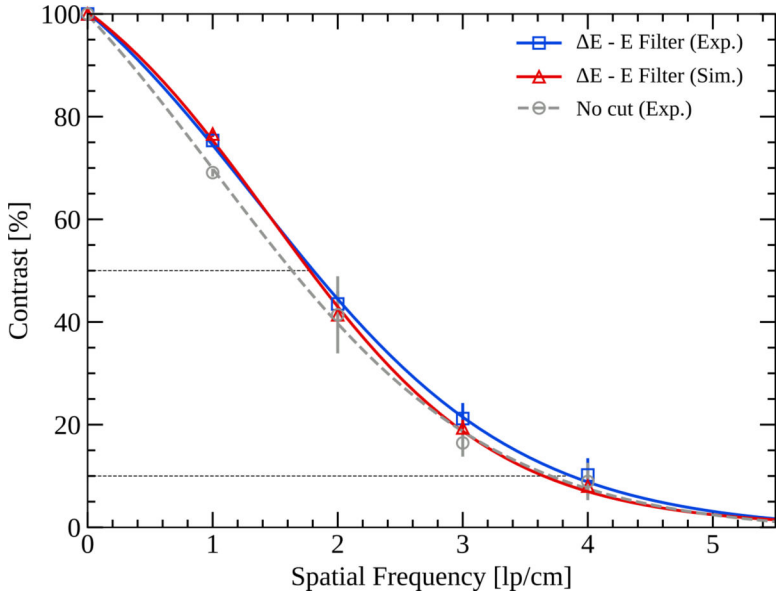

Figure 11.

MTF of the experimentally acquired (blue) and simulated (red) HeCT of the CTP528 module with the $\Delta E - E$ filter applied. The dashed gray line shows the MTF of the experimentally acquired HeCT without filtering secondaries before reconstruction. The error bars mark the standard deviation of the measured contrast. A sigmoid fit has been performed to yield the MTF over the whole spatial frequency range. The dashed lines indicate the $MTF_{50\%}$ and $MTF_{10\%}$, respectively.